

*promoting access to White Rose research papers*



**Universities of Leeds, Sheffield and York**  
**<http://eprints.whiterose.ac.uk/>**

---

This is an author produced version of a paper published in **Semiconductor Science and Technology**

White Rose Research Online URL for this paper:

<http://eprints.whiterose.ac.uk/74861/>

---

**Published paper:**

Dean, P, Salih, M, Khanna, SP, Li, LH, Saat, NK, Valavanis, A, Burnett, AD, Cunningham, JE, Davies, AG and Linfield, EH (2012) *Resonant-phonon depopulation terahertz quantum cascade lasers and their application in spectroscopic imaging*. *Semiconductor Science and Technology*, 27 (9).

<http://dx.doi.org/10.1088/0268-1242/27/9/09400>

4

---

# Resonant–phonon depopulation terahertz quantum cascade lasers and their application in spectroscopic imaging

**P Dean, M Salih, S P Khanna, L H Li, N K Saat, A Valavanis, A Burnett, J E Cunningham, A G Davies, and E H Linfield**

School of Electronic and Electrical Engineering, University of Leeds, Leeds, LS2 9JT, UK

Email: p.dean@leeds.ac.uk

**Abstract** The terahertz (THz) frequency quantum cascade laser (QCL) is a semiconductor heterostructure laser that has attracted much research interest over the past decade. We report on the high performance of THz QCLs based on a three-well resonant-phonon (RP) depopulation active region (AR) and operating in the frequency range 2.7 THz to 4.0 THz. Devices, processed into surface-plasmon waveguides, lased up to 116 K in pulsed mode with threshold current densities as low as  $840 \text{ Acm}^{-2}$ . The effects of the design frequency and laser cavity length on performance are discussed. We also report on the operation of QCLs with reduced AR thicknesses, and show, for the first time, that the AR thickness of RP QCLs processed in a surface plasmon waveguide can be reduced to as little as  $5 \mu\text{m}$ . Finally, we demonstrate the use of an electrically tuneable THz QCL, based on a heterogeneous AR, for spectroscopic imaging of the high-explosive pentaerythritol tetranitrate.

## 1. Introduction

The quantum cascade laser (QCL) [1] is a semiconductor laser consisting of a repeated stack of multiple quantum well heterostructures. Unlike interband lasers, in which photon generation is accomplished by electron–hole recombination across the material band gap, QCLs are *unipolar* devices that make use of intersubband transitions only. This approach, which was first proposed in 1971 [2], enables the generation of photons at energies significantly below the material band gap. Of particular significance, QCLs provide access to the terahertz (THz) region of the electromagnetic spectrum (frequency  $f \sim 300 \text{ GHz}–10 \text{ THz}$ ; wavelength  $\lambda \sim 1000–30 \mu\text{m}$ ; energy  $\sim 1–40 \text{ meV}$ ), which is historically the least explored region of the spectrum owing to the difficulties associated with the development of suitable radiation sources at these frequencies. Such spectral coverage of QCLs makes them potentially suitable for a range of applications across the physical and biological sciences [3,4].

Despite early concerns about the possible detrimental effects of optical phonon emission at low temperatures, the first QCL was demonstrated above the phonon energy, at a wavelength  $\lambda = 4.2 \mu\text{m}$  ( $f = 71 \text{ THz}$ ), in the GaInAs/AlInAs material system [1]. Mid-infrared QCLs have subsequently become established as the principal semiconductor source of high-power coherent radiation in the region  $\lambda = 3–24 \mu\text{m}$  [5,6,7]. It was not until 2002, however, that the first QCL emitting below the optical phonon energy was reported [8]. This initial THz QCL was based on a GaAs/AlGaAs chirped

superlattice active region (AR) and was capable of emitting  $>2\text{mW}$  of peak power at 4.4 THz, albeit with a low average power of  $\sim 5\ \mu\text{W}$ . Furthermore, the maximum operating temperature of this first structure QCL was only 50 K.

Since this time, THz QCLs have witnessed remarkable development. To date, devices have been demonstrated with emission frequencies ranging from 1.2 to 5.0 THz [9,10], and with operating temperatures as high as 199.5 K in pulsed mode [11]. Under continuous wave operation output powers exceeding 100 mW have also been achieved [12]. Central to these advances has been the design and engineering of a range of AR schemes, most notably the bound-to-continuum (BTC) [13] and resonant-phonon (RP) [14,15] designs. The latter exploits fast electron-optical-phonon scattering to depopulate the lower lasing level – an approach that enables a population inversion to be maintained up to high operating temperatures, at which thermal backfilling [16] of the lower lasing state prevents operation of alternative AR schemes. Nevertheless, despite enabling high temperature operation, RP schemes typically suffer from the presence of strong parasitic current channels that artificially enhance the threshold current [17,18]. In addition, owing to the requirement to drop  $>36\ \text{meV}$  (the LO phonon energy in GaAs) across each individual module of the RP structure, large applied biases are required at threshold. Both of these factors lead to large electrical power dissipation in RP QCLs, making continuous wave operation challenging. The BTC design, which typically exhibits low threshold current densities, is therefore most frequently employed for applications requiring continuous wave operation.

Over the past decade there has been significant development of THz QCL-based spectroscopy and imaging systems, driven by the opportunities presented by the unique properties of THz radiation. Unlike millimetre-waves, THz radiation excites vibrational modes in many organic and inorganic materials, enabling samples to be discriminated chemically as well as providing sensitivity to differences in crystalline structure [19,20]. THz radiation is also non-ionising and is able to penetrate dry non-polar materials such as paper and plastic packaging, thereby enabling concealed sample investigation. These properties make THz radiation particularly suitable to a range of applications including non-destructive inspection, security screening, and biomedicine, as well as atmospheric science and astronomy [3,4]. Examples of THz QCL-based systems include compact imaging [21] and displacement sensing [22] schemes utilising the self-mixing effect in QCLs, diffuse reflection [23,24] and transmission [25] imaging systems for spectroscopic sample analysis, imaging systems for biomedical applications [26] and non-destructive evaluation [9], as well as heterodyne mixing schemes [27,28] for applications including high-resolution gas spectroscopy [29].

One consideration in the development of THz QCLs for applications is the choice of waveguide. Devices with the highest operating temperatures and lowest threshold current densities make use of a metal-metal (MM) waveguide in which the AR heterostructure is sandwiched between metallic layers [30]. The result is almost total confinement of the waveguide mode within the AR. However, owing to the sub-wavelength aperture in this type of waveguide (typically  $\sim 10\ \mu\text{m}$  thick compared to  $\lambda \sim 100\ \mu\text{m}$  in free-space), the output beam experiences strong diffraction. The resulting beam patterns [31] are extremely poor, rendering this waveguide unsuitable for many of the potential applications of THz QCLs. Several approaches have been demonstrated to improve the beam properties of such devices, including second- [32] and third-order [33] distributed feedback gratings, photonic crystal waveguides [34], coupling to horn antennas [35,36] and spoof surface plasmon structures [37]. An alternative approach, though, is to use a semi-insulating surface plasmon (SP) waveguide [8], as utilised in the first THz QCLs. This waveguide is simpler to fabricate, has a better

output beam profile, and typically emits higher output powers compared with MM structures. In this case a surface plasmon mode is loosely bound to a metallic layer on top of the AR and a heavily-doped  $n^+$  region beneath, which itself is grown on a semi-insulating substrate. Owing to the reduced overlap of the waveguide mode with doped semiconductor and metallic layers, the SP waveguide exhibits lower waveguide losses compared to MM waveguides. More significantly, though, is the far superior beam quality and lower beam divergence demonstrated [38]. The majority of THz QCL-based systems developed to date have consequently employed the SP waveguide .

The ability to accurately tailor the emission frequency of THz QCL devices greatly improves their applicability across a range of areas, particularly applications in spectroscopic analysis, including gas spectroscopy. The study of the accessible frequency range of existing AR schemes is therefore of particular importance. In this paper we present experimental results from SP devices incorporating four AR designs, each based on a three-well RP depopulation scheme, that have been tailored to provide emission frequencies of  $\sim 4.0$  THz,  $\sim 3.4$  THz,  $\sim 3.1$  THz and  $\sim 2.7$  THz. For each AR, the measured emission frequencies, threshold current densities, maximum operating temperatures and range of operating voltages are compared for a number of Fabry-Pérot ridge lasers of different cavity lengths. THz QCLs emitting at 3.1 THz are also reported with reduced AR thicknesses, and we show, for the first time, that the AR thickness of RP QCLs processed in a SP waveguide can be reduced to as little as 5  $\mu\text{m}$ .

We then demonstrate the use of an electrically tuneable THz QCL based on a heterogeneously cascaded RP scheme for multiple-frequency spectroscopic imaging. The spectral properties of this laser are presented, demonstrating that quasi-single mode emission can be achieved at five frequencies in the range 3.06–3.35 THz through control of the driving bias. Transmission images of pressed pellets of the high explosive pentaerythritol tetranitrate (PETN) are finally reported, acquired at these five frequencies with a single two-dimensional scan of the sample.

## 2. Device design and fabrication

The THz QCL devices used in this work are based on a robust GaAs/AlGaAs three-well RP depopulation scheme [15] that has recently been optimised to operate at temperatures as high as 199.5 K in pulsed mode when processed in a MM waveguide [11]. Wafers were grown by molecular beam epitaxy [39], typically to a thickness of 10  $\mu\text{m}$ . Table 1 shows the layer sequences for one period of four ARs tailored to provide emission frequencies of  $\sim 4.0$  THz,  $\sim 3.4$  THz,  $\sim 3.1$  THz and  $\sim 2.7$  THz. Figure 1 shows the conduction band diagram for two units of the  $\sim 3.1$  THz QCL design. The lasing transition is between states 4 and 3, with the injector state 1 providing fast electron-optical-phonon extraction from state 2.

Each AR was grown between doped upper 80-nm-thick ( $n = 5 \times 10^{18} \text{ cm}^{-3}$ ) and lower 700-nm-thick ( $n = 5 \times 10^{18} \text{ cm}^{-3}$ ) GaAs contact layers. The wafers were then processed into identical laser cavities with a SP waveguide using the method outlined in Ref. 39. Briefly, optical lithography was used for defining the laser ridges and ohmic contacts. The thicknesses of the Au/Ge/Ni bottom and top contacts were  $\sim 200$  nm and  $\sim 100$  nm, respectively, and the thickness of the Ti/Au overlayer was  $\sim 20$  nm/ $\sim 200$  nm. A  $\sim 150$   $\mu\text{m}$  ridge width was used for all devices and the cleaved device facets were left uncoated.

## 3. QCLs operating in the range 2.7–4.1 THz

In the four AR designs studied, the total number of quantum wells/barriers and the doping levels ( $n = 5 \times 10^{16} \text{ cm}^{-3}$ ) were kept constant. The relative performance of each device is therefore expected to be strongly dependent on the AR design frequency as well as the cavity length. Indeed, a strong dependence of device performance on the design frequency has previously been described for RP QCL devices fabricated with MM waveguides [18].

For characterization the devices were mounted on the cold-finger of a continuous-flow cryostat equipped with polyethylene windows. Radiation was collected and coupled into a helium-cooled silicon bolometer using two off-axis parabolic reflectors in a nitrogen purged atmosphere. Emission spectra were acquired with a resolution of 7.5 GHz using a Bruker IFS-66 Fourier-transform spectrometer. Devices were operated in pulsed mode with a pulse width of 2  $\mu\text{s}$  and a repetition rate of 10 kHz.

Figure 2 shows typical emission spectra obtained for the four ARs from devices with dimensions  $\sim 1.5 \text{ mm} \times 150 \mu\text{m}$ , acquired at a heat-sink temperature of 15 K. The lasing frequency was found to scale principally with the width of the AR quantum wells, in agreement with simulations.

Figure 3 summarizes the variation of the threshold current density ( $J_{\text{th}}$ ) with cavity length ( $L$ ) for the four ARs with  $L = 0.6\text{--}2.8 \text{ mm}$ . The lowest threshold current densities are obtained for devices in the range  $L \sim 1.3\text{--}1.8 \text{ mm}$ , with the absolute lowest value ( $J_{\text{th}} \sim 840 \text{ Acm}^{-2}$ ) being realized in the  $\sim 3.1 \text{ THz}$  AR design. In general, however, similar thresholds ( $\sim 900\text{--}1000 \text{ Acm}^{-2}$ ) are observed for all cavity lengths in the three higher-frequency ARs. Notably  $J_{\text{th}}$  is significantly larger ( $\sim 1075 \text{ Acm}^{-2}$ ) for devices operating at  $\sim 2.7 \text{ THz}$ . In this respect it should be noted that comparison between QCL devices fabricated from different wafers can be challenging, owing to varying growth conditions including background doping levels. Nevertheless, the enhanced threshold observed at 2.7 THz appears consistent with the analysis presented in Ref. 18. The performance of low-frequency three-well RP devices is limited by the parasitic current; at higher frequencies optical phonon scattering of thermal electrons is the limiting factor. Using the parameter values obtained in Ref. 18 it can be seen that, at 2.7 THz and for low electron temperatures (estimated to be 50 K above the 15 K heat sink temperature in our case), the parasitic current channel greatly exceeds the injection current in the upper lasing level at threshold. Measured values of the parasitic current indicate a  $\sim 40 \pm 20 \%$  increase from 2.7 THz to 3.1 THz, which agrees very well with the  $\sim 30\%$  increase in threshold current density observed in our devices. Furthermore, reduced confinement of the optical mode within the AR must be considered for the case of SP waveguides. When compounded with the difficulty in achieving selective injection and the greater free-carrier losses (which scale as  $\lambda^2$ ) [40] at low frequencies, the inferior performance of the 2.7 THz devices is broadly as expected. Indeed, devices with  $L < 1.2 \text{ mm}$  were found not to lase for this AR, whereas lasing was observed for shorter devices at the three higher frequencies. Moreover, devices at 2.3 THz were found not to lase. Table 2 summarizes the range of operating voltages for exemplar devices from each of the four AR designs. It can be seen that a significantly reduced operating range is exhibited at the lowest operating frequency, again attributed to the closely spaced energy levels in this design. As a result, the negative differential resistance region, and consequently the cessation of lasing, occurs at a lower bias.

The maximum operating temperatures  $T_{\text{max}}$  measured for each of the four ARs as a function of cavity length are shown in figure 4. Once again, the largest  $T_{\text{max}}$  is achieved in devices in the range  $L \sim 1.3\text{--}1.8 \text{ mm}$  for all four lasing frequencies. The largest values of  $T_{\text{max}}$  were found to be similar

(~110 K to ~115 K) for the 4.0 THz, 3.4 THz and 3.1 THz devices of optimum length, but lower (86 K) in the case of the 2.7 THz structure.

The observed dependencies of  $J_{th}$  and  $T_{max}$  on the cavity length are mutually consistent, with optimum performance being accomplished for devices with cavity lengths  $L \sim 1.3\text{--}1.8$  mm. This lower limit is attributed to the relative contributions of mirror and waveguide losses. Specifically, in shorter devices the effective mirror losses become significant in comparison to the gain and waveguide losses, leading to an increased threshold current density [42]. Conversely, whilst the effective mirror losses become less significant in longer devices, greater driving currents are required at the alignment field. Peak electrical powers  $>35$  W at threshold are typical for devices with  $L > 2$  mm, which will lead to an increased lattice temperature. This could account for the degraded performance observed in longer devices, although further measurements would be required to verify this. Nevertheless, this work suggests that further reduction in the emission frequency using the three-well phonon-depopulation scheme with SP waveguides should be possible with judicious choice of the cavity length.

#### 4. THz QCLs with reduced active region thickness

The THz QCLs reported to date have typically used active regions of  $\sim 10$   $\mu\text{m}$  thickness; this represents a compromise between a number of factors. First, as the structure thickness is increased, it becomes more difficult to achieve uniformity in the MBE growth rate over the AR and hence obtain identical quantum well/barrier thicknesses. It also adds to the time and cost of the epitaxial growth. Nevertheless, an increase in the AR thickness would improve the overlap between the optical mode and AR in SP waveguides, as well as the output beam profile and coupling efficiency. However, such advantages are partially negated by the requirement for higher operating voltages to achieve the requisite threshold electric fields. This, in turn, would lead to larger electrical power dissipation in the AR, resulting in device heating.

In general, the affect of parasitic heating is compounded in RP structures by the large parasitic current channels [17,18] inherent in this AR design. As a result continuous-wave operation is difficult to achieve, which is problematic for many applications including the use of THz QCLs in heterodyne mixing schemes. For this reason, we studied the behaviour of a series of 3.1 THz three-quantum RP QCL designs in which the AR thickness was reduced from 10 to 5  $\mu\text{m}$ . A similar study has been reported for THz QCLs processed with MM waveguides [43], in which it was shown that the AR thickness could be reduced to as little as 1.75  $\mu\text{m}$  owing to the strong vertical confinement in this type of waveguide. In addition to reducing the influence of device heating, having a thinner AR potentially offers the benefit of easier future integration with other THz opto-electronic components.

A series of QCLs were fabricated based on the 3.1 THz three-quantum RP design with AR thicknesses of 10, 7.5, and 5  $\mu\text{m}$ ; the number of periods in the three ARs being 226, 170 and 113. Figure 5 shows typical power-current density-voltage characteristics for these three ARs. It should be noted that the voltages plotted here contain a contribution from the device contact resistances. In the absence of these series resistances, the voltages dropped across each AR are expected to scale with the number of periods. The device dimensions were 1.53 mm  $\times$  150  $\mu\text{m}$  for the 10  $\mu\text{m}$  AR, 1.55 mm  $\times$  150  $\mu\text{m}$  for the 7.5  $\mu\text{m}$  AR and 1.58 mm  $\times$  200  $\mu\text{m}$  for the 5  $\mu\text{m}$  AR; a wider ridge was used for the 5  $\mu\text{m}$  case in order to reduce waveguide losses, since 150  $\mu\text{m}$  wide ridges were found not to lase. It can be seen that the threshold current density increases from  $\sim 950$   $\text{Acm}^{-2}$  to  $\sim 1200$   $\text{Acm}^{-2}$  as the AR thickness decreases from 10  $\mu\text{m}$  to 5  $\mu\text{m}$ . The maximum operating temperature is found to

correspondingly decrease from 115 K to 66 K, with the maximum peak output power at 15 K falling from ~20 mW to ~2.5 mW.

This degradation of performance in thinner ARs is attributed primarily to the progressively reduced overlap of the waveguide mode with the AR. The threshold current density can be related to the waveguide losses  $\alpha_W$ , the mirror losses  $\alpha_M$  and the modal overlap (confinement) factor  $\Gamma$  according to the analytic expression

$$J_{th} = J_p + \frac{\alpha_W + \alpha_M}{\Gamma g_{th}} = J_p + \frac{G_{th}}{g_{th}} \quad (1)$$

where  $g_{th}$  and  $G_{th}$  are the gain coefficient and the gain at threshold, and  $J_p$  is the parasitic current density. Simulations of the SP waveguide performed using a two-dimensional finite element model (COMSOL), with complex permittivities of the waveguide layers obtained from the bulk Drude model, indicate that  $\Gamma$  for the 10, 7.5, and (200- $\mu\text{m}$  wide) 5  $\mu\text{m}$  ARs are 0.32, 0.26 and 0.19, respectively. As can be seen from (1), the gain experienced by the SP waveguide mode will scale correspondingly. The total waveguide losses ( $\alpha_W + \alpha_M$ ) are calculated to be 18  $\text{cm}^{-1}$ , 20  $\text{cm}^{-1}$  and 22  $\text{cm}^{-1}$  for 10, 7.5, and 5  $\mu\text{m}$  ARs, respectively. Overall these values indicate that the threshold gain increases from 56  $\text{cm}^{-1}$  for the 10  $\mu\text{m}$  AR to 116  $\text{cm}^{-1}$  for the 5  $\mu\text{m}$  AR. The proportionally smaller increase in  $J_{th}$  observed is a consequence of the parasitic current channel. In addition, the range of operating voltages for the 10- $\mu\text{m}$ -thick AR was ~6.6 V, whereas for the 5  $\mu\text{m}$  AR the value was only ~3.5 V. The fact that these voltages do not scale with AR thickness is attributed to the greater threshold field for the thinner structures, which is a direct consequence of the increased threshold current density in thinner devices. Nevertheless, these results demonstrate that the AR thickness of RP QCLs processed in a SP waveguide can be reduced to as low as 5  $\mu\text{m}$ . Thin ARs such as this are less demanding on the MBE growth technology and also enable devices to be operated at reduced biases.

## 5. Heterogeneous THz QCL for spectroscopic imaging applications

### 5.1. Characterisation of heterogeneous THz QCL

As we have demonstrated above, through careful engineering of the quantum well and barrier widths the emission frequency of THz QCL sources can be controlled. Nevertheless, for many potential applications of THz QCLs there is a need to control the lasing frequency electrically within a single device. This approach offers considerable advantages over the use of multiple sources, primarily by eliminating the difficulties associated with multiple source alignment, and also considerably simplifying system design.

Our approach to developing an electrically tuneable THz QCL is based on the sequential stacking of multiple three-well RP AR designs in a single device. In our structure, which has been described in detail elsewhere [44], the gallium growth rate was systematically reduced by ~10% during (molecular beam) epitaxial growth of the AR. This results in a ‘‘heterogeneous cascade’’ AR consisting of 23 sections of 10 repeated periods; the first section of 10 periods was grown with a gallium growth rate of 1.064  $\mu\text{m}/\text{hr}$ , the second set at 1.059  $\mu\text{m}/\text{hr}$ , and each subsequent set was grown with a further 0.5% reduction in the growth rate until finally a rate of 0.94  $\mu\text{m}/\text{hr}$  was attained for the final twenty-third section. Consequently, the GaAs well thickness is reduced by ~10% through the AR. In addition, the mole fraction of aluminium in the barriers increases from 14.2% to 15.7% and the Si doping level from  $4.7 \times 10^{16} \text{ cm}^{-3}$  to  $5.3 \times 10^{16} \text{ cm}^{-3}$  over the AR. By varying the bias applied to this structure, emission in the frequency range ~3.05 THz to ~3.40 THz can be achieved.

The QCL used for this study was fabricated in a SP waveguide with ridge dimensions  $2.1 \text{ mm} \times 140 \text{ }\mu\text{m} \times 10 \text{ }\mu\text{m}$ . Whilst SP waveguide structures preclude the high-temperature operation possible with MM waveguides, the improved beam quality and smaller beam divergence associated with the SP waveguide lend themselves well to imaging applications, as discussed above. The device was cooled to 15 K using a helium-cooled continuous-flow cryostat, and driven with 2  $\mu\text{s}$  current pulses at a repetition rate of 10 kHz. Figure 6(a) shows the current-voltage and light-current characteristics measured under these conditions. This device operates up to a temperature of 85 K in pulsed mode, making possible the exploitation of liquid nitrogen cooling. The emission spectra of the device obtained at five different driving biases are shown in figure 6(b). For these biases, emission is achieved predominantly at frequencies of 3.06, 3.18, 3.24, 3.30 and 3.35 THz. This tuning behaviour is attributed to the sequential switching of different lasing-units as the bias is increased. As the well thicknesses are reduced, the lasing transition shifts to higher energies, and greater electric fields are required to attain alignment in the structure.

### 5.2. Spectroscopic imaging

The imaging system used for our work has been described in detail elsewhere [25]. Briefly, radiation from the QCL was collimated and focussed onto the sample. The transmitted radiation was collected and coupled into a helium-cooled silicon bolometer. For image acquisition the sample was mounted on a computer-controlled two-axis translation stage and raster-scanned with a step-size of 250  $\mu\text{m}$ . At each sample position the QCL driving bias was switched between the five chosen biasing conditions (see figure 6(b)), and the detector response recorded for each bias. The 10 kHz train of driving pulses was modulated at a frequency of  $\sim 190$  Hz, with lock-in detection used to improve the detection sensitivity. Samples of the high explosive pentaerythritol tetranitrate (PETN) were prepared by diluting with polytetrafluoroethylene (PTFE) to 26% by volume (26 vol %) and mechanical pressing into pellets of diameter 8 mm and thickness  $\sim 0.5$  mm. The volume fraction of PETN used is restricted to  $< 26\%$  to prevent explosion during sample preparation.

The transmission images of the 26 vol % PETN pellet acquired at each frequency are shown in figure 7. The image size is  $44 \times 44$  pixels, corresponding to an area measuring  $11 \text{ mm} \times 11 \text{ mm}$ , and the images have been normalised to the maximum transmitted power. The mean sample transmittance was measured by sampling over a  $5 \text{ mm} \times 5 \text{ mm}$  ( $20 \times 20$  pixels) region in the centre of the pellet to reduce the effects of laser speckle and inhomogeneity within the sample. Figure 8 shows the sample attenuation coefficients calculated at each frequency following the analysis described in Ref. 25. The uncertainty in these values has been estimated from the variance of the 400 sampled pixel values. For comparison, the attenuation coefficients measured using broadband THz time-domain spectroscopy [45] are also shown – these give good agreement with the values obtained using the THz QCL. The spectrum of PETN exhibits a strong resonant absorption peaked at  $\sim 2.85$  THz [46], which gives rise to a decreasing attenuation with increasing frequency in the range 2.9 THz to 3.7 THz, as seen in figure 8.

The current imaging setup could potentially be developed further through the use of liquid nitrogen cooling, although the present non-optimised heterogeneous QCL would likely suffer from a reduced operating range, and hence reduced tuneability at higher temperatures. The helium-cooled bolometer could also be substituted for a sensitive room temperature detector such as a Golay cell or Schottky diode. Overall, such developments would enable a more compact system that is not reliant on liquid helium cooling and is thus more suited to spectroscopic imaging applications [47].

## 6. Summary

The performance of THz QCLs based on a three-well resonant-phonon depopulation active region and operating in the range 2.7 THz to 4.0 THz has been reported for devices processed with a SP waveguide. It has been shown that the threshold current density and maximum operating temperature depend critically on the AR design and the device length. The best overall performance was observed at a frequency of 3.1 THz and the optimum performance was achieved for cavity lengths  $L \sim 1.3$ – $1.8$  mm at all four frequencies tested. As a consequence of the lack of confinement and greater waveguide losses in the SP waveguide, the lower frequency limit for achieving lasing in this AR design is likely to be just below the 2.7 THz measured in this work. The lower limit on the operating frequency of RP devices fabricated with SP waveguides will have implications for the implementation of such devices in spectroscopic imaging and sensing systems. THz QCLs emitting at 3.1 THz have also been demonstrated with reduced AR thicknesses. These results indicate that the AR thickness of RP QCLs processed in a SP waveguide can be reduced to as low as  $5 \mu\text{m}$ . Thin ARs such as this are less demanding on the MBE growth technology and also enable devices to be operated at reduced biases. Furthermore, we have demonstrated spectroscopic imaging of the high-explosive PETN using an electrically tuneable THz QCL in the range 3.06–3.35 THz. This work demonstrates the applicability of THz QCL sources to spectroscopic imaging.

We are grateful for support from the EPSRC, the ERC (*NOTES* and *TOSCA* programmes), the Royal Society, the Wolfson Foundation, the Government of Malaysia, and the Innovative Research Call in Explosives and Weapons Detection (2007), a cross-government programme sponsored by a number of government departments and agencies under the CONTEST strategy.

**Table 1.** The GaAs/Al<sub>0.15</sub>Ga<sub>0.85</sub>As layer sequence and thicknesses (starting from the injection barrier) for RP QCLs with four different emission frequencies. Barriers are indicated in bold. The uniformly doped GaAs layer ( $\text{Si} = 5 \times 10^{16} \text{ cm}^{-3}$ ) is underlined.

Frequency (THz)	Layer sequence (Å)
4.0	<b>47</b> /99/ <b>15</b> /73/ <b>40</b> /55/ <u>54</u> /55
3.4	<b>47</b> /98/ <b>17</b> /74/ <b>41</b> /54/ <u>54</u> /54
3.1	<b>48</b> /96/ <b>20</b> /74/ <b>42</b> /53/ <u>55</u> /53
2.7	<b>48</b> /94/ <b>24</b> /72/ <b>42</b> /51/ <u>55</u> /51

**Table 2.** The voltage operating range for four exemplar THz QCL devices with different emission frequencies. The voltages at the threshold ( $V_{\text{th}}$ ) and cessation ( $V_{\text{OFF}}$ ) of lasing are also shown.

Frequency (THz)	$L$ (mm)	$V_{\text{th}}$ (V)	$V_{\text{OFF}}$ (V)	Operating range (V)
4.0	1.38	13.0	>19.2 <sup>a</sup>	>6.2 <sup>a</sup>
3.4	1.52	11.6	18	6.4
3.1	1.51	12.8	19.0	6.2
2.7	1.56	12.8	16.2	3.4

<sup>a</sup> Cessation of lasing was not reached.

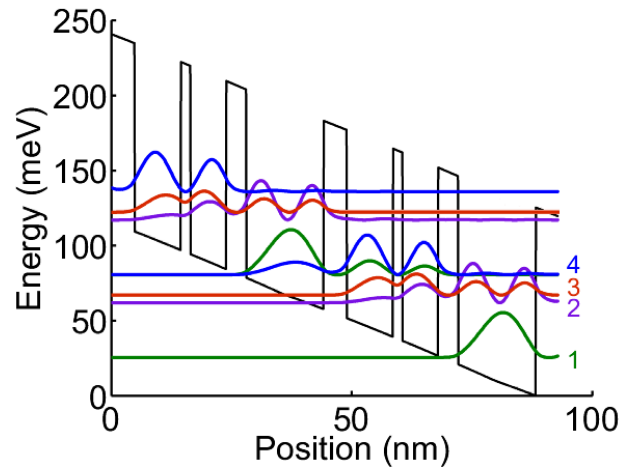


**Figure 1.** Conduction band diagram for two units of the 3.1 THz three-well RP QCL under an applied bias of  $12.5 \text{ kVcm}^{-1}$ , with the squared magnitude of the wavefunctions illustrated. The layer sequence is described in Table 1. The radiative transition is from state 4 to state 3. Electrons are depopulated from state 2 by fast electron-phonon scattering to the injector state 1.

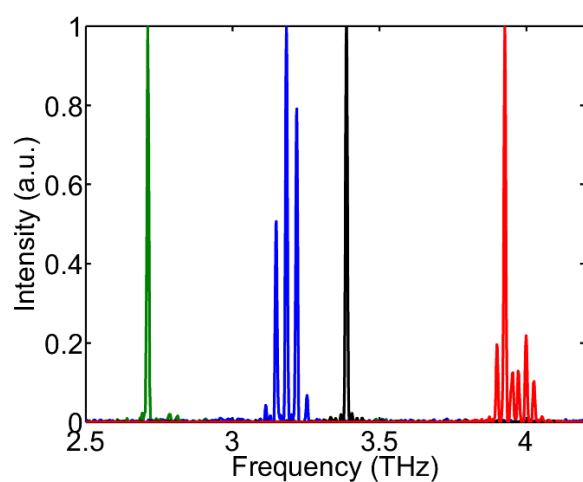


**Figure 2.** Emission spectra of four different RP QCL ARs tailored to emit at different frequencies through engineering of the quantum well widths. The device dimensions were  $\sim 1.5 \text{ mm} \times 150 \text{ }\mu\text{m}$ , and spectra were acquired at a heat-sink temperature of 15 K.

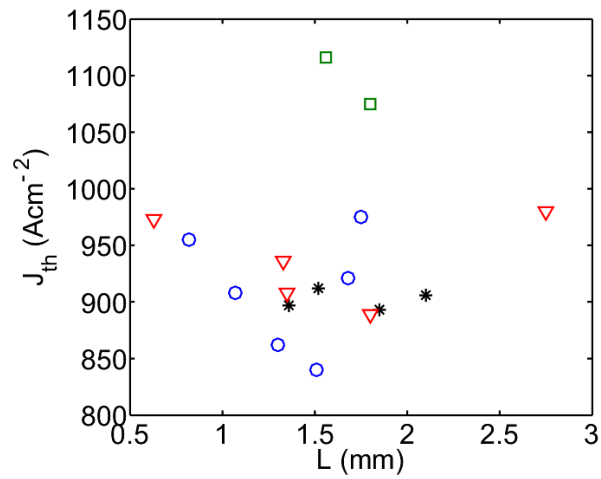


**Figure 3.** Threshold current densities  $J_{th}$  measured at 15 K for devices of different cavity length  $L$ , for RP ARs emitting at ~4.0 THz (red triangles), ~3.4 THz (black asterisks), ~3.1 THz (blue circles) and ~2.7 THz (green squares). All devices were 150  $\mu\text{m}$  wide

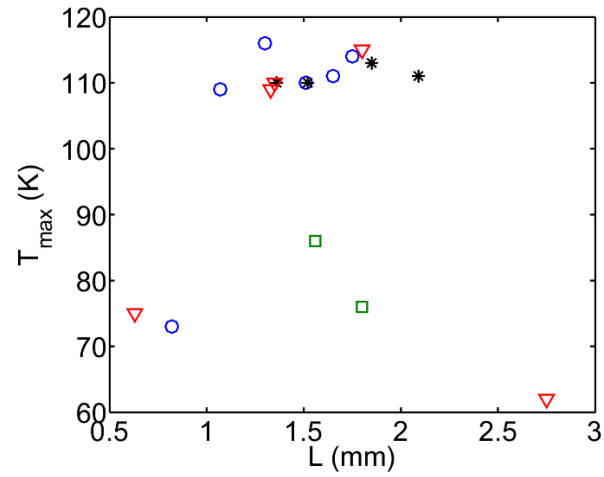


**Figure 4.** Maximum operating temperatures ( $T_{\max}$ ) for devices of different cavity length  $L$ , for RP ARs emitting at ~4.0 THz (red triangles), ~3.4 THz (black asterisks), ~3.1 THz (blue circles) and ~2.7 THz (green squares). All devices were 150  $\mu\text{m}$  wide.

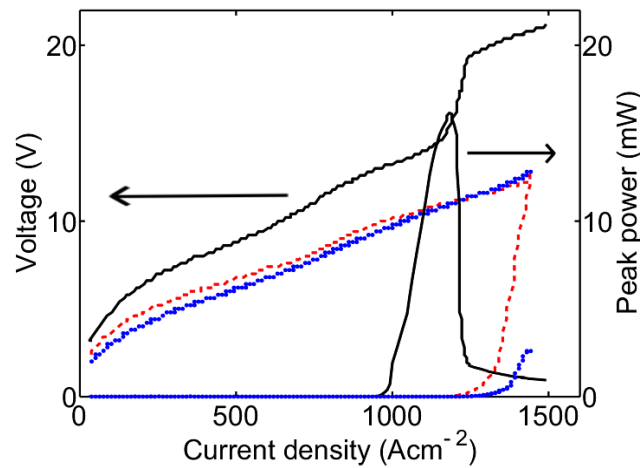


**Figure 5.** Peak power (right axis) and voltage (left axis) as a function of current density for 3.1 THz three-well RP QCLs with AR thicknesses of 10  $\mu\text{m}$  (black, solid line), 7.5  $\mu\text{m}$  (red, dashed line), and 5  $\mu\text{m}$  (blue, dashed-dotted line). The device dimensions were 1.53 mm  $\times$  150  $\mu\text{m}$  for the 10  $\mu\text{m}$  AR, 1.55 mm  $\times$  150  $\mu\text{m}$  for the 7.5  $\mu\text{m}$  AR and 1.58 mm  $\times$  200  $\mu\text{m}$  for the 5  $\mu\text{m}$  AR.

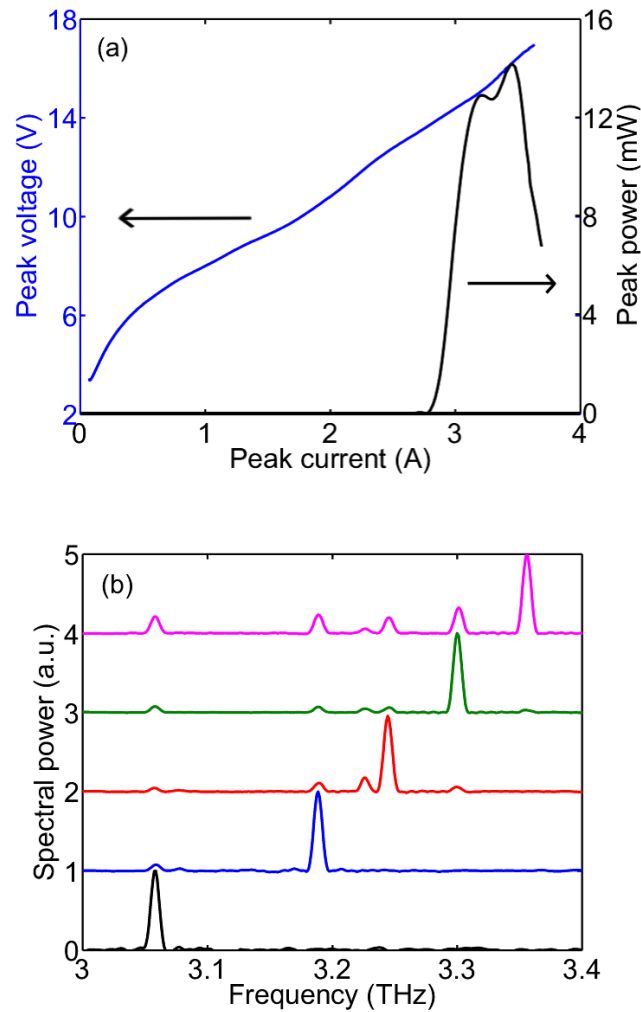


**Figure 6.** (a) Peak power (right axis) and voltage (left axis) as a function of current density for a RP QCL based on a heterogeneous AR. (b) Normalised emission spectra obtained under five different biases and a heat sink temperature of 15 K. The device dimensions are  $2.1 \text{ mm} \times 140 \text{ }\mu\text{m} \times 10 \text{ }\mu\text{m}$ .

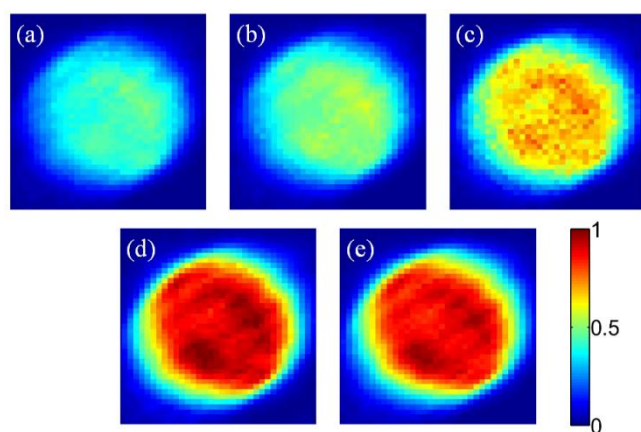


**Figure 7.** Transmission images of a pellet containing 26 vol % PETN taken at frequencies of (a) 3.06 THz, (b) 3.18 THz, (c) 3.24 THz, (d) 3.30 THz, and (e) 3.35 THz. The total image area is 11 mm  $\times$  11 mm and the step size is 0.25 mm. The colour scale has been normalised to the maximum transmitted power.

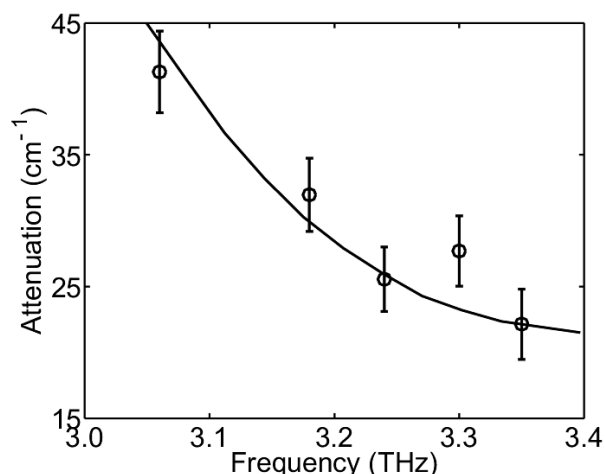


**Figure 8.** Attenuation coefficient (circles) as a function of frequency for a pellet containing 26 vol % PETN. The error bars have been estimated from the variance of the sampled image pixels. The attenuation spectrum obtained from broadband THz time-domain spectroscopy is also shown (solid line).

## References

- [1] Faist J, Capasso F, Sivco D L, Sirtori C, Hutchinson A L and Cho A Y 1994 Quantum cascade laser *Science* **264** 553–556
- [2] Kazarinov R F and Suris R A 1971 Possibility of the amplification of electromagnetic waves in a semiconductor with a superlattice *Sov. Phys. Semiconductors* **5** 707–9
- [3] Mittleman D 2003 *Sensing with Terahertz Radiation* (Springer, Berlin)
- [4] Tonouchi M 2007 Cutting-edge terahertz technology *Nature Photonics* **1** 97–105
- [5] Revin D G, Cockburn J W, Steer M J, Airey R J, Hopkinson M, Krysa A B, Wilson L R, Menzel S 2007 InGaAs/AlAsSb/InP quantum cascade lasers operating at wavelengths close to 3  $\mu\text{m}$  *Appl. Phys. Lett.* **90** 021108
- [6] Semtsiv M P, Wienold M, Dressler S and Masselink W T 2007 Short-wavelength ( $\lambda \approx 3.05 \mu\text{m}$ ) InP based strain-compensated quantum-cascade laser *Appl. Phys. Lett.* **90** 051111
- [7] Colombelli R, Capasso F, Gmachl C, Hutchinson A L, Sivco D L, Tredicucci A, Wanke M C, Sergent A M and Cho A Y 2001 Far-infrared surface-plasmon quantum-cascade lasers at 21.5  $\mu\text{m}$  and 24  $\mu\text{m}$  wavelengths *Appl. Phys. Lett.* **78** 2620–2
- [8] Köhler R, Tredicucci A, Beltram F, Beere H E, Linfield E H, Davies A G, Ritchie D A, Iotti R C and Rossi F 2002 Terahertz semiconductor-heterostructure laser *Nature* **417** 156–159
- [9] Kumar S and Lee A W M 2008 Resonant-phonon terahertz quantum cascade lasers and video-rate terahertz imaging *IEEE J. Sel. Topics Quantum Electron.* **14** 333–44
- [10] Scalari G, Walther C, Fischer M, Terazzi R, Beere H, Ritchie D and Faist J 2009 THz and sub-THz quantum cascade lasers *Laser Photon. Rev.* **3**, 45–66
- [11] Fatholouloumi S, Dupont E, Chan C W I, Wasilewski Z R, Laframboise S R, Ban D, Mátyás A, Jirauschek C, Hu Q and Liu H C 2012 Terahertz quantum cascade lasers operating up to  $\sim 200$  K with optimized oscillator strength and improved injection tunnelling *Optics Express* **20** 3866–76
- [12] Williams B, Kumar S, Hu Q, and Reno J L 2006 High-power quantum cascade lasers *Electron. Lett.* **42** 89–90
- [13] Barbieri S, Alton J, Beere H E, Fowler J, Linfield E H and Ritchie D A 2004 2.9 THz quantum cascade laser operating up to 70 K in continuous wave *Appl. Phys. Lett.* **85** 1674–6
- [14] Williams B S, Callebaut H, Kumar S, Hu Q and Reno J L 2003 3.4-THz quantum cascade laser based on longitudinal-optical-phonon scattering for depopulation *Appl. Phys. Lett.* **82** 1015–7
- [15] Luo H, Laframboise S R, Wasilewski Z R, Aers G C, Liu H C and Cao J C 2007 Terahertz quantum-cascade laser based on a three-well active module *Appl. Phys. Lett.* **90** 041112
- [16] Williams B S 2007 Terahertz quantum-cascade lasers *Nature Photon.* **1** 517–25
- [17] Callebaut H, Kumar S, Williams B S, Hu Q and Reno J L 2003 Analysis of transport properties of terahertz quantum cascade lasers *Appl. Phys. Lett.* **83** 207–9

- 
- [18] Chassagneux Y, Wang Q J, Khanna S P, Strupiechonski E, Coudeville J-R, Linfield E, Davies A G, Capasso F, Belkin M and Colombelli R 2012 Limiting Factors to the Temperature Performance of THz Quantum Cascade Lasers Based on the Resonant-Phonon Depopulation Scheme *IEEE Transactions on THz Science and Technology* **2** 83–92
- [19] Davies A G, Burnett A D, Fan W, Linfield E H and Cunningham J E 2008 Terahertz spectroscopy of explosives and drugs *Materials Today* **11** 18–26
- [20] Zeitler J A, Taday P F, Newnham D A, Pepper M, Gordon K C and Rades T 2007 Terahertz pulsed spectroscopy and imaging in the pharmaceutical setting - a review *J. Pharm. Pharmacol.* **59** 209–223
- [21] Dean P *et al.* 2011 Terahertz imaging through self-mixing in a quantum cascade laser *Optics Letters* **36** 2587–9
- [22] Lim Y L *et al.* 2011 Demonstration of a self-mixing displacement sensor based on terahertz quantum cascade lasers *Appl. Phys. Lett.* **99** 081108
- [23] Dean P, Shaikat M U, Khanna S P, Chakraborty S, Lachab M, Burnett A D, Davies A G and Linfield E H 2008 Absorption-sensitive diffuse reflection imaging of concealed powders using a terahertz quantum cascade laser *Optics Express* **16** 5997–6007
- [24] Dean P, Burnett A, Tych K, Khanna S, Lachab M, Cunningham J, Linfield E H and Davies A G 2011 Measurement and analysis of the diffuse reflectance of powdered samples at terahertz frequencies using a quantum cascade laser *Journal of Chemical Physics* **134** 134304
- [25] Dean P, Saat N K, Khanna S P, Salih M, Burnett A, Cunningham J, Linfield E H and Davies A G 2009 Dual-frequency imaging using an electrically tunable terahertz quantum cascade laser *Optics Express* **17** 20631–41
- [26] Kim S M, Hatami F, Harris J S, Kurian A W, Ford J, King D, Scalari G, Giovannini M, Hoyler N, Faist J and Harris G 2006 Biomedical terahertz imaging with a quantum cascade laser *Appl. Phys. Lett.* **88** 153903–5
- [27] Khosropanah P, Zhang W, Hovenier J N, Gao J R, Klapwijk T M, Amanti M I, Scalari G and Faist J 2008 3.4 THz heterodyne receiver using a hot electron bolometer and a distributed feedback quantum cascade laser *J. Appl. Phys.* **104** 113106
- [28] Hajenius M, Khosropanah P, Hovenier J N, Gao J R, Klapwijk T M, Barbieri S, Dhillon S, Filloux P, Sirtori C, Ritchie D A and Beere H E 2008 Surface plasmon quantum cascade lasers as terahertz local oscillators *Optics Letters* **33** 312–4
- [29] Hübers H W, Pavlov S G, Richter H, Semenov A D, Mahle L, Tredicucci A, Beere H E and Ritchie D A 2006 High-resolution gas phase spectroscopy with a distributed feedback terahertz quantum cascade laser *Appl. Phys. Lett.* **89** 061115
- [30] Williams B S, Kumar S, Callebaut H, Hu Q and Reno J L 2003 Terahertz quantum-cascade laser at  $\lambda \approx 100$   $\mu\text{m}$  using metal waveguide for mode confinement *Appl. Phys. Lett.* **83** 2124–7
- [31] Adam A J L, Kasalynas I, Hovenier J N, Klaassen T O, Gao J R, Orlova E E, Williams B S, Kumar S, Hu Q and Reno J L 2006 Beam patterns of terahertz quantum cascade lasers with subwavelength cavity dimensions *Appl. Phys. Lett.* **88** 151105
- [32] Fan J A, Belkin M A, Capasso F, Khanna S, Lachab M, Davies A G and Linfield E H 2006 Surface emitting terahertz quantum cascade laser with a double-metal waveguide *Opt. Express* **14** 11672–80
- [33] Amanti M I, Fischer M, Scalari G, Beck M and Faist J 2009 Low divergence single-mode terahertz quantum cascade laser *Nature Photonics* **3** 586–90
- [34] Chassagneux Y, Colombelli R, Mainault W, Barbieri S, Beere H E, Ritchie D A, Khanna S P, Linfield E H and Davies A G 2009 Electrically pumped photonic-crystal terahertz lasers controlled by boundary conditions *Nature* **457** 174–8
- [35] Lloyd-Hughes J, Scalari G, Kolck A, Fischer M, Beck M and Faist J 2009 Coupling terahertz radiation between sub-wavelength metal-metal waveguides and free space using monolithically integrated horn antennae *Optics Express* **17** 18387–93
- [36] Amanti M I, Fisher M, Walther C, Scalari G, Faist J 2007 Horn antennas for terahertz quantum cascade lasers *Elec. Lett.* **43** 573–4
- [37] Yu N, Wang Q J, Kats M A, Fan J A, Khanna S P, Li L, Davies A G, Linfield E H and Capasso F 2010 Designer spoof surface plasmon structures collimate terahertz laser beams *Nature Materials* **9** 730–5
- [38] Richter H, Semenov A D, Pavlov S G, Mahler L, Tredicucci A, Beere H E, Ritchie D A, Il'in K S, Siegel M and Hübers H-W 2008 Terahertz heterodyne receiver with quantum cascade laser and hot electron bolometer mixer in a pulse tube cooler *Appl. Phys. Lett.* **93** 141108
- [39] Khanna S P, Chakraborty S, Lachab M, Hinchcliffe N M, Linfield E H and Davies A G 2008 The growth and measurement of terahertz quantum cascade lasers *Physica E* **40** 1859–61
- [40] Kohen S, Williams B S and Hu Q 2005 Electromagnetic modeling of terahertz quantum cascade laser waveguides and resonators *Appl. Phys. Lett.* **97** 053106

- [42] Gmachl C, Capasso F, Sivco D and Cho A 2001 Recent progress in quantum cascade lasers and applications *Rep. Prog. Phys.* **64** 1533–1601
- [43] Strupiechonski E, Grassani D, Fowler D, Julien F H, Khanna S P, Li L, Linfield E H, Davies A G, Krysa A B and Colombelli R 2011 Vertical subwavelength mode confinement in terahertz and mid-infrared quantum cascade lasers *Appl. Phys. Lett.* **98** 101101
- [44] Khanna S P, Salih M, Dean P, Davies A G and Linfield E H 2009 Electrically tunable terahertz quantum-cascade laser with a heterogeneous active region *Appl. Phys. Lett.* **95** 181101
- [45] Fan W H, Burnett A D, Upadhyaya P C, Cunningham J E, Linfield E H and Davies A G 2007 Far-infrared spectroscopic characterization of explosives for security applications using broadband terahertz time-domain spectroscopy *Applied Spectroscopy* **61** 638–43
- [46] Chen J, Chen Y, Zhao H, Bastiaans G J and Zhang X –C 2007 Absorption coefficients of selected explosives and related compounds in the range of 0.1–2.8 THz *Opt. Express* **15** 12060–7
- [47] Bründermann E, Havenith M, Scalfari G, Giovannini M, Faist J, Kunsch J, Mechold L and Abraham M 2006 Turn-key compact high temperature terahertz quantum cascade lasers: imaging and room temperature detection *Optics Express* **14** 1829–41